Check for updates

Enhanced mechanical quality factor of BiScO₃–PbTiO₃ piezoelectric ceramics using glass composition

Hongwei Shi,[ab] Zujian Wang, [ID][a] Xiaoming Yang,[a] Rongbing Su,[a] Xifa Long [ID] *[ab] and Chao He [ID] *[ab]

Compared with pure Pb-based perovskite ferroelectric materials, Bi(Me)O₃–PbTiO₃ (Me = Sc^{3+}, In^{3+}, Yb^{3+}) have attracted attention due to their remarkable advantage in their Curie temperature. Among them, BiScO₃–PbTiO₃ piezoelectric ceramic is a potential piezoelectric material in high-temperature applications for its high Curie temperature and excellent piezoelectric coefficient. However, its shortcomings are high dielectric loss and low mechanical quality factor. Herein, we report the improvement of the mechanical quality factor of 0.36BS–0.64PT ceramics through the addition of glass composition (GeO₂). There is a small change in the Curie temperature after GeO₂ addition. The piezoelectric coefficient d_{33} and planar electromechanical coupling factor k_p increase first and then decrease, and the mechanical quality factor Q_m monotone increases with an increase in GeO₂. The 0.36BS–0.64PT + 0.5 mol%GeO₂ ceramics have optimal electrical properties with T_C of 455 °C, d_{33} of 385 pC N⁻¹, k_p of 58%, and Q_m of 90. In addition, the thermal stability of 0.36BS–0.64PT + xGeO₂ and 0.36BS–0.64PT ceramics is almost the same. It was concluded that the mechanical quality factor of BS–PT ceramics can be enhanced by the addition of GeO₂ with other properties remaining unchanged.

1. Introduction

With the requirement of high-temperature piezoelectric sensors and actuators in aerospace, automobiles, oil and gas exploration fields, high-temperature piezoelectric materials have received unprecedented attention.[1–4] The use temperature of piezoelectric materials is about half of the Curie temperature (T_C) due to piezoelectric performance degradation at high temperatures.[5] The commercial lead–zirconium–titanium (PZT) piezoelectric ceramics have been studied for decades and are widely used in piezoelectric sensors and transducers, but these ceramics cannot be used in environments above 200 °C, while applications in the aerospace and automotive industries require piezoelectric devices to operate at a temperatures of 300 °C or higher.[6,7] Therefore, the development of new high-temperature-stable piezoelectric materials is an extremely urgent need.

Bismuth-based perovskite solid solutions with the formula of Bi(Me)O₃–PbTiO₃ (Me = Sc, In, Yb, Mg/Ti, Fe, Ga *et al.*), which are potential alternatives for high-temperature application, have attracted growing interest due to their ultra-high Curie temperature.[8–13] Among them, BiYbO₃–PbTiO₃, BiInO₃–PbTiO₃, Bi(Mg₁/₂Ti₁/₂)O₃–PbTiO₃ and BiFeO₃–PbTiO₃ are not suitable for

applications due to their poor piezoelectric properties. BiScO₃–PbTiO₃ (BS–PT) solid solutions have drawn considerable attention because of their high piezoelectric constant (d_{33}) of 460 pC N⁻¹ and high T_C of 450 °C near the morphotropic phase boundary (MPB).[14,15] In addition, due to the advantages of high working efficiency, good flexibility, high strength and toughness of flexible ceramic film materials, some researchers have focused on preparing multifunctional materials on flexible substrates. For example, Liu successfully fabricated Mn–In₂O₃ thin films with excellent mechanical durability and transparent conductive oxide SrVO₃ thin films by pulsed laser deposition (PLD) on flexible substrates.[16,17] BS–PT solid solutions have small crystal anisotropy and excellent electrical performance, which can be combined with a flexible substrate to improve the piezoelectric response.[18]

The shortcomings of BS–PT ceramics are high dielectric loss (tan δ > 3%) and a low mechanical quality factor (Q_m < 30),[19,20] which limit their application at high temperatures. Previously, a great deal of work has been done to increase the Q_m of BS–PT ceramics through chemical methods, such as the addition of Mn, Fe, Pb(Mn₁/₃Nb₂/₃)O₃, Pb(Mn₁/₃Sb₂/₃)O₃.[4,21–25] The mechanical quality factor can be enhanced by chemical methods, while the piezoelectric performance and Curie temperature are often decreased. For example, the piezoelectric performance of (0.97-x)BiScO₃–xPbTiO₃–0.03Pb(Mn₁/₃Nb₂/₃)O₃ ceramics deteriorated severely (d_{33} < 300 pC N⁻¹).[24] The Curie temperature of 0.03Pb(Mn₁/₃Sb₂/₃)O₃–0.33BS–0.64PT and

[a]Key Laboratory of Optoelectronic Materials Chemistry and Physics, Fujian Institute of Research on the Structure of Matter, Chinese Academy of Sciences, Fuzhou, 350002, China. E-mail: hechao@fjirsm.ac.cn; lxf@fjirsm.ac.cn

[b]University of Chinese Academy of Sciences, Beijing, 100049, China

BiScO$_3$–PbTiO$_3$–Pb(Yb$_{1/2}$Nb$_{1/2}$)O$_3$ ceramics is less than 400 °C.[23,26] Mn and Fe co-modified BS–PT ceramics show both a lower d_{33} of 235 pC N^{-1} and dielectric constant ε_r of 815 compared with pure BS–PT ceramics.[25]

GeO$_2$–glass former is an additive used in glass. This glass former can decrease the dielectric loss and increase insulativity. Ge^{4+} ions tend to segregate along the grain boundaries, leading to a reduction in the jumping of mobile ions, which in turn causes a decrease in the conductivity of the ceramics.[27] Mou *et al.* used Ge^{4+} to enhance the piezoelectric performance and adjusted dielectric properties.[28] GeO$_2$ can synchronously enhance the Q_m and piezoelectric properties in the KNN and BCZT system.[29,30] Therefore, we investigated the effect of GeO$_2$ addition on the phase structure, dielectric, piezoelectric, ferroelectric and electromechanical coupling properties of BS–PT ceramics.

2. Experimental procedures

The GeO$_2$ doped 0.36BS–0.64PT piezoelectric ceramics (abbreviated as 0.36BS–0.64PT + xGeO$_2$, x = 0 mol%, 0.25 mol%, 0.5 mol%, 0.75 mol%, 1.0 mol%, 1.5 mol%) were prepared by the conventional solid-state reaction method. Starting materials were Bi$_2$O$_3$ (99.99%), Sb$_2$O$_3$ (99.99%), PbO (99.9%), TiO$_2$ (99.5%), and GeO$_2$ (99.99%). These oxide powders were weighed and mixed according to the chemical formula, adding 1 mol% Bi$_2$O$_3$ and PbO to compensate for evaporation during the sintering process. The mixture was ball milled for 12 h in absolute ethyl alcohol (99.7%) with zirconia balls, then dried and pressed into pellets at 60 MPa. The pellets were placed in a crucible and calcined at 780 °C for 5 h at a heating/cooling rate of 5 °C min^{-1}. Thereafter, the GeO$_2$ of different amounts was added to the calcined powder and ball milled again for another 24 h. After ball milling, the slurry was dried, crushed, and mixed with 5% polyvinyl alcohol binder (PVA). The powder was passed through a 200 mesh sieve and was pressed into pellets of 8 mm in diameter and 1.5 mm in thickness under an actual pressure of 200 MPa. Subsequently, it was heated at 600 °C for 2 h to eliminate the binder, and sintered in a sealed Al$_2$O$_3$ crucible in the range of 1000–1100 °C for 2 h to form ceramic samples.

The crystal structure of sintered ceramics was analyzed on an X-ray diffractometer (Rigaku, Miniflex600, Japan) with Cu-Kα radiation. The TEM was performed using a field emission transmission electron microscope (TEM, FEI Tecnai F20, USA). A scanning electron microscope (SEM, SU8010, Hitachi, Japan) was used to investigate the microstructure. The density of the sintered samples was determined by the Archimedes method. The obtained ceramics were polished to a thickness of 0.5 mm, and then coated with silver paste on the surface to form the electrodes. The samples were poled in an oil bath at 120 °C in an electric field of 40 kV cm^{-1} for 15 min. After standing for 24 h, the electrical properties were tested. The dielectric constant (ε_r) and dielectric loss (tan δ) were measured on an impedance analyzer (E4990A, Agilent Technologies, USA), and the planar electromechanical coupling factor (k_p) and Q_m were calculated according to the resonance and anti-resonance method. Ferroelectric hysteresis loop measurements were performed on an aix-ACCT TF2000 ferroelectric analyzer (f = 1 Hz). Piezoelectric coefficients were measured by a quasi-static d_{33} meter (Institute of Acoustics, Chinese Academy of Sciences, model ZJ-4AN).

3. Results and discussion

3.1 Structure and phase analysis

Fig. 1(a) shows the X-ray diffraction patterns (log scale) of powder 0.36BS–0.64PT + xGeO$_2$ ceramics. The main peaks of all samples matched with the perovskite phase, indicating formed stable perovskite solid solutions. It can be easily seen that the second phase (GeO$_2$) appeared as the doping content of GeO$_2$ increased, indicating that it is difficult for Ge^{4+} to enter the lattice. The radius of Ge^{4+} ion (0.53 Å for CN = 6) is almost similar to that of Ti^{4+} ions (0.605 Å for CN = 6), and it is considered that Ge^{4+} ions can enter the B site of the perovskite unit cell and substitute Ti^{4+} ions.[31] Fig. 1(b) shows the amplified images of (200)$_c$ peaks. It can be easily seen that the phase structure is slightly changed after adding GeO$_2$. The lattice parameters of 0.36BS–0.64PT + xGeO$_2$ ceramics were calculated according to the diffraction patterns, as shown in Fig. 1(c). With the increase in the GeO$_2$ content, the "c" value decreases continuously while the "a" value increases, and the c/a value keeps decreasing from 1.023 to 1.014, which confirms that the Ge^{4+} ion entered the B site of the perovskite unit cell.

Fig. 2 shows the TEM image of 0.36BS–0.64PT + 0.5GeO$_2$ ceramics. One set of lattice fringes with an interplanar spacing
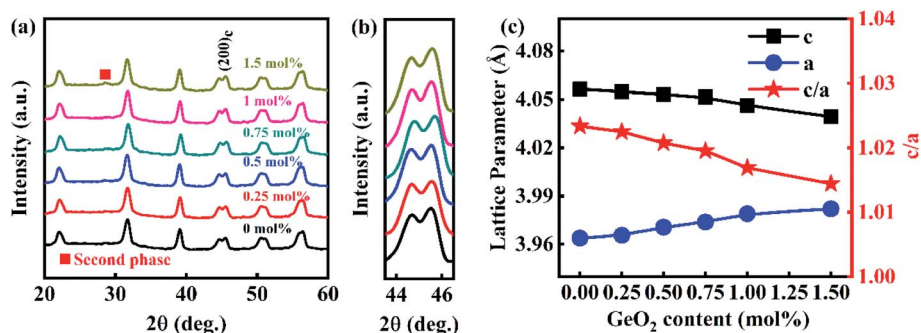

Fig. 1 (a) X-ray diffraction patterns (log scale) of powder 0.36BS–0.64PT + xGeO$_2$ ceramics. (b) The amplified images of (200)$_c$ peaks. (c) Lattice parameters of 0.36BS–0.64PT + xGeO$_2$ ceramics.
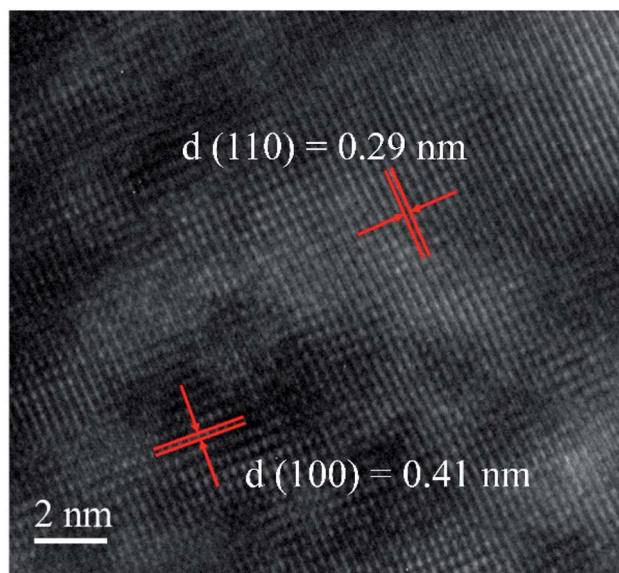
Fig. 2 TEM image of 0.36BS−0.64PT + 0.5GeO$_2$ ceramics.

of 0.29 nm, corresponding to the (110) plane of the perovskite phase, and another set of lattice fringes with a 0.41 nm interplanar spacing, corresponding to the (100) plane of the perovskite phase, which consistent with the phase structure shown by the XRD results.

Fig. 3 shows the microstructure of 0.36BS−0.64PT + xGeO$_2$ ceramics sintered at 1080 °C for 2 h. These images clearly show the morphology of the ceramic samples with few holes, dense grains and clear grain boundaries. Table 1 lists the density of the 0.36BS−0.64PT + xGeO$_2$ ceramics. The actual density (ρ_1) was calculated by the Archimedes method, and the theoretical density (ρ_2) was calculated according to XRD data. The relative density (ρ_r) is 96.17–97.82%, showing a high density. The insets of Fig. 3 show the statistical data of the grain size of 0.36BS−0.64PT + xGeO$_2$ ceramics. With the increase in GeO$_2$, the average grain size decreases from 8.46 μm to 2.54 μm, indicating that GeO$_2$ can inhibit the growth of grains. A similar phenomenon has been reported in other Ge doped ceramics. Fig. 3(e and f) show that a small amount of GeO$_2$ gathers at the grain boundary, which hinders the movement of the grain
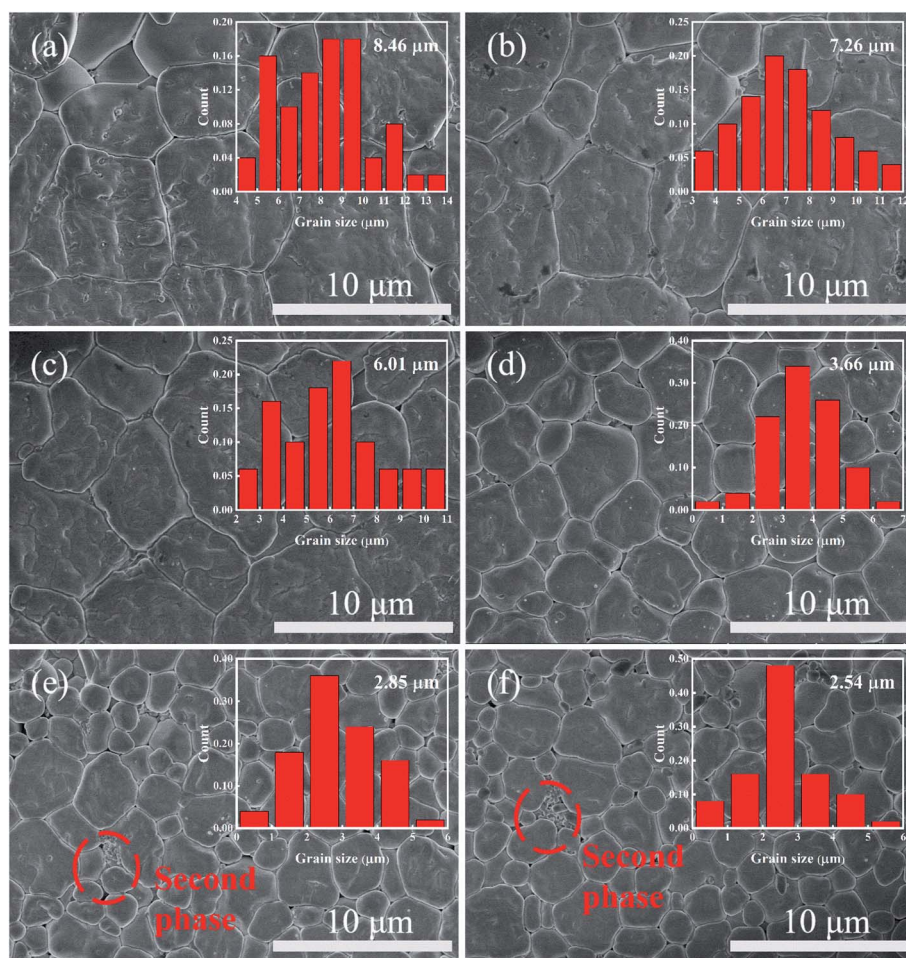

Fig. 3 SEM images of the surface of 0.36BS−0.64PT + xGeO$_2$ ceramics sintered at 1080 °C: (a) 0 mol% (b) 0.25 mol%, (c) 0.5 mol%, (d) 0.75 mol%, (e) 1.0 mol%, (f) 1.5 mol%. The insets show the statistical data of the grain size of 0.36BS−0.64PT + xGeO$_2$ ceramics.

RSC Advances

Table 1 The variation in the density of 0.36BS−0.64PT + xGeO$_2$ ceramics (ρ_1: actual density; ρ_2: theoretical density; ρ_r: relative density)

x (mol%)	ρ_1 (g cm^{-3})	ρ_2 (g cm^{-3})	ρ_r (%)
0.00	7.53	7.83	96.17
0.25	7.58	7.82	96.93
0.50	7.64	7.81	97.82
0.75	7.61	7.80	97.56
1.00	7.58	7.79	97.30
1.50	7.52	7.79	96.53

boundary and restrains the grain growth. The results show that Ge^{4+} cannot be dissolved into the solid solution.

3.2 Dielectric properties

Fig. 4 shows the temperature dependence of ε_r and tan δ of 0.36BS−0.64PT + xGeO$_2$ ceramics. The temperature of the maximum of dielectric constant (T_m) is considered as the Curie temperature (T_C).[23] Table 2 summarizes the ε_r, tan δ and T_C of

0.36BS−0.64PT + xGeO$_2$ ceramics. The T_C of 0.36BS−0.64PT ceramics with 0, 0.25, 0.5, 0.75, 1 and 1.5 mol% GeO$_2$ are 449, 457, 455, 454, 458 and 462 °C, respectively, showing a small change of GeO$_2$. The decrease in c/a indicates that the crystal structure shifts to the rhombohedral phase, and the Curie temperature should be reduced in theory. However, compared with the undoped BS–PT ceramic samples, the introduction of GeO$_2$ slightly increases the Curie temperature. It is indicated that the addition of GeO$_2$ is good for stabilizing the Curie temperature.

The values of ε_r at room temperature increased first and then decreased with the increase in GeO$_2$, as shown in Table 2. The maximum ε_r observed when x = 0.5 mol% was 1280. An increase in the dielectric constant is related to an increase in density. The addition of GeO$_2$ to 0.36BS−0.64PT ceramics can improve the microstructure of the material. In addition, the GeO$_2$ doping is beneficial to reducing the dielectric loss.

It can be easily seen that all the samples exhibit a diffuse phase transition. The variation of the diffuse phase transition
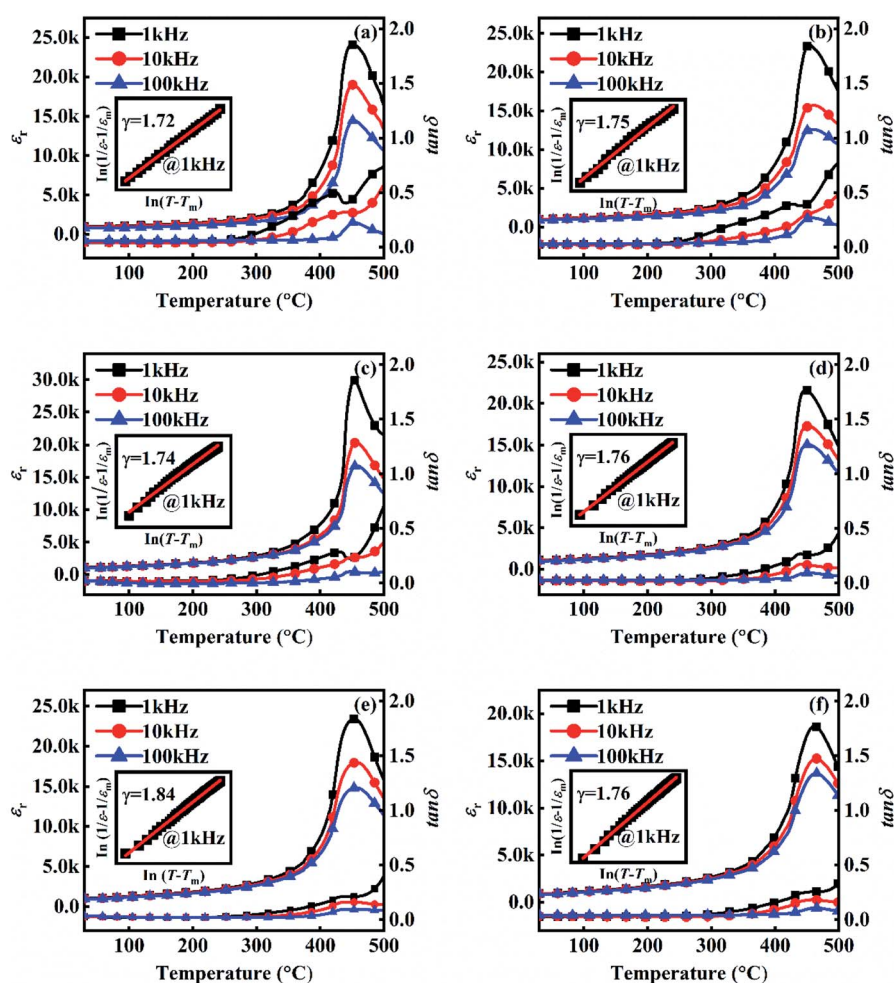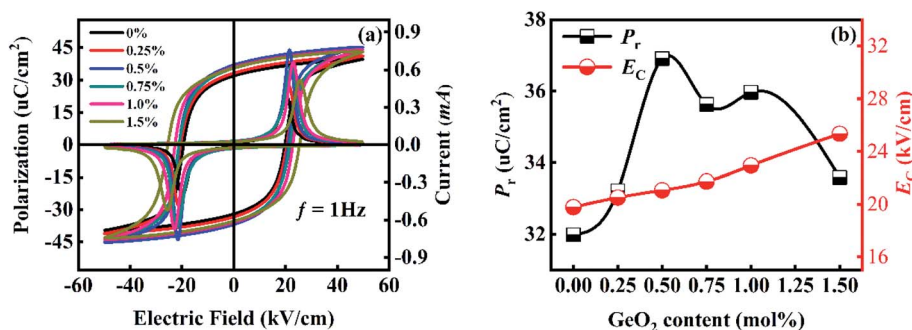

Fig. 4 Temperature dependence of ε_r and tan δ of 0.36BS−0.64PT + xGeO$_2$ ceramics: (a) 0 mol% (b) 0.25 mol%, (c) 0.5 mol%, (d) 0.75 mol%, (e) 1.0 mol%, (f) 1.5 mol%. The insets show the fitting results using the semi-empirical Curie−Weiss law.

Table 2 Electrical properties of 0.36BS−0.64PT + xGeO$_2$ ceramics at room temperature

x (mol%)	T_C (°C)	ε_r (@1k Hz)	tan δ (%)	E_C (kV cm^{-1})	P_r (μC cm^{-2})	d_{33} (pC N^{-1})	k_p	Q_m
0.00	449	1130	3.31	19	32	355	0.49	28
0.25	457	1150	1.47	20	33	370	0.53	75
0.50	455	1280	1.18	21	37	385	0.58	90
0.75	454	1240	1.44	22	36	335	0.55	101
1.00	458	1200	1.71	23	36	305	0.54	115
1.50	462	1070	1.97	25	35	270	0.52	132

Fig. 5 (a) $P–E$ loops and $I–E$ loops, (b) the variation of P_r and E_C of 0.36BS−0.64PT + xGeO$_2$ ceramics.

with increase in GeO$_2$ was explored. The diffuse phase transition can be described by the modified Curie–Weiss law:[32]

$$\ln(1/\varepsilon - 1/\varepsilon_m) + \ln C = \gamma \ln(T - T_m) \qquad (1)$$

where C is the Curie Weiss constant, ε_m is the value of ε_r at T_m, and γ is the degree of phase transition diffuses. When γ is equal to 1, it is usually regarded as a normal ferroelectricity. For $\gamma = 2$, the relaxor ferroelectric completely diffuses the phase transition. Alternatively, the larger the γ value, the greater the degree of diffuse phase transition. The inset in Fig. 4 shows the fitting curve at 1 kHz of the 0.36BS−0.64PT + xGeO$_2$ ceramics, showing that the value of γ for all the ceramic samples is in the range of 1.72–1.84, indicating a strong relaxation behavior. The relaxor behavior is related to the heterogeneity of the solid solution. The complex ions occupy both the A-site (Bi, Pb) and B-site (Ti, Sc, Ga) in the perovskite structure, leading to a disordered distribution of ions.[33] Therefore, the value of γ reflects the degree of heterogeneity. The close values of γ indicate that the GeO$_2$ addition does not vary the degree of heterogeneity, which is consistent with the stability of the Curie temperature.

3.3 Ferroelectric and piezoelectric properties

Fig. 5(a) shows the $P–E$ loops and $I–E$ loops of 0.36BS−0.64PT + xGeO$_2$ ceramics measured at room temperature with 1 Hz. According to the $P–E$ hysteresis loops, the variation of the values of remnant polarization (P_r) and coercive field (E_c) was obtained, as shown in Fig. 5(b) and Table 2. The P_r value of the virgin BS–PT ceramics is 32 μC cm^{-2}. The P_r values increase significantly when a small amount of GeO$_2$ is added. 0.36BS−0.64PT + 0.5 mol%GeO$_2$ ceramics have the maximum P_r value (37 μC

cm^{-2}). When the GeO$_2$ added is higher than 0.50 mol%, the value of P_r decreases slightly because of the glass phase formed by the addition of GeO$_2$. The value of E_c gradually increases as the GeO$_2$ content increases, indicating the enhanced breakdown strength.

Fig. 6 shows the variation trend of piezoelectric coefficient (d_{33}), planar electromechanical coupling factor (k_p), and mechanical quality factor (Q_m) of the 0.36BS−0.64PT + xGeO$_2$ ceramics. The detailed data of d_{33}, k_p, Q_m are listed in Table 2. As shown in Fig. 6, the d_{33} and k_p of 0.36BS−0.64PT + xGeO$_2$ ceramics increased first and then decreased. The maximum value of d_{33} and k_p is 385 pC N^{-1}, 58% at $x = 0.50$ mol%, which is higher than that of the virgin BS–PT ceramics (355 pC N^{-1}, 49%). The enhanced piezoelectric performance is attributed to the combined effect of the grain size. The piezoelectric
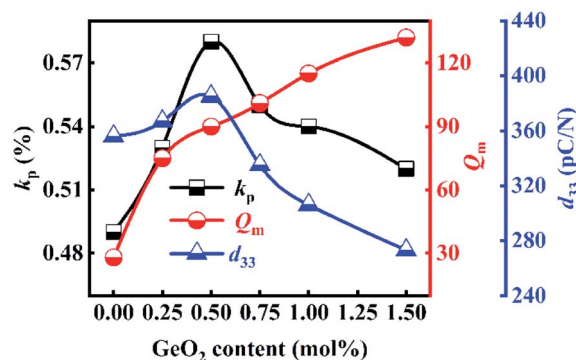
Fig. 6 The variation of k_p, Q_m and d_{33} of 0.36BS−0.64PT + xGeO$_2$ ceramics.
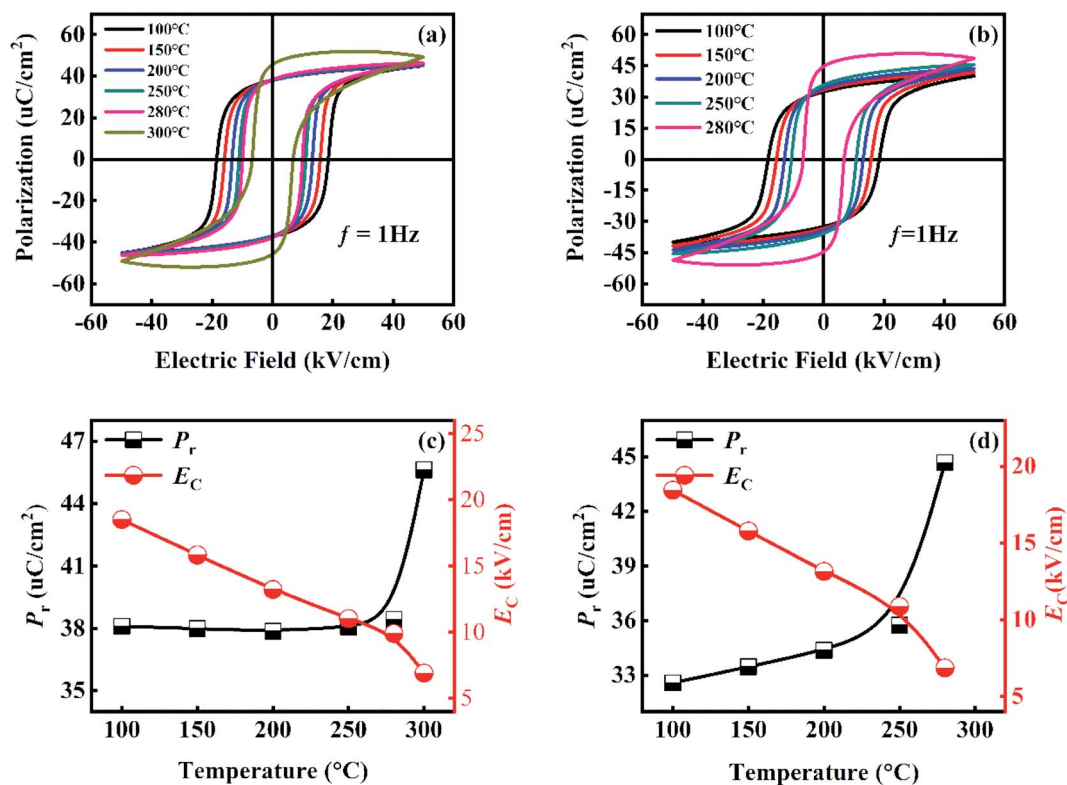
Fig. 7 Temperature dependence of (a and b) P–E loops, and (c and d) P_r and E_c for (a and c) 0.36BS–0.64PT + 0.5 mol%GeO$_2$ and (b and d) 0.36BS–0.64PT ceramics.

performance decreased as the GeO$_2$ content increased beyond 0.50 mol%. The addition of GeO$_2$ can obstruct the movement of the domain and reduce the external contribution to piezoelectricity, resulting in a decrease in d_{33}.[29] Interestingly, the Q_m value of ceramic increased monotonically with the increase in the GeO$_2$ concentration. It is concluded that the addition of GeO$_2$ can improve the mechanical quality factor, which is consistent with the variation of E_c.

3.4 Thermal stability

Thermal stability is valuable for sensors and actuators in various industrial applications. Fig. 7 shows the temperature dependence of P–E loops of the 0.36BS–0.64PT + 0.5 mol%GeO$_2$ and 0.36BS–0.64PT. All curves were measured under an electric field of 50 kV cm^{-1} with a frequency of 1 Hz. As the temperature increased, the P–E loops of 0.36BS–0.64PT + 0.5 mol%GeO$_2$ ceramics still maintained a good rectangular loop at 280 °C without obvious leakage conductance. When the temperature rose to 300 °C, the leakage current was too large to form a saturated P–E loop confirmed by the abnormal high value of P_r (see Fig. 7(a)). The variation of the P_r and E_c of 0.36BS–0.64PT + 0.5 mol%GeO$_2$ ceramics are shown in Fig. 7(c). The E_c decreased from 19 kV cm^{-1} at 100 °C to 10 kV cm^{-1} at 280 °C, while the P_r remained almost unchanged. The clear leakage conductance appears at 280 °C for 0.36BS–0.64PT ceramics, as shown in Fig. 7(b and d), which is consistent with literature that BS–PT ceramics begin to degrade at 250 °C.[34] The temperature stability

of piezoelectric devices based on BS–PT ceramics is only 250 °C.[35,36] Therefore, it is indicated that the addition of GeO$_2$ is in favor of the enhancement of the thermal stability of BS–PT ceramics.

To further characterize the temperature stability of the samples, the poling samples were annealed at different temperatures for one hour, and their d_{33} was measured again at room temperature (Fig. 8). It can be easily seen that the d_{33} of 0.36BS–0.64PT ceramics starts decreasing above 250 °C.
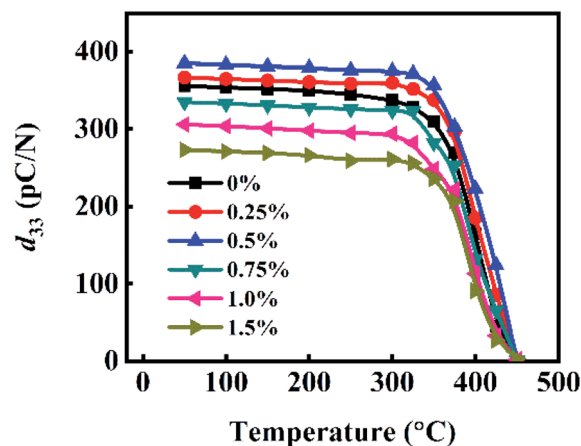

Fig. 8 The thermal stability of d_{33} of 0.36BS–0.64PT + xGeO$_2$ ceramics.

Compared with 0.36BS–0.64PT ceramics, the 0.36BS–0.64PT + 0.5 mol%GeO_2 ceramics exhibit unchanged d_{33} above 300 °C. This indicates that GeO_2 addition improves the piezoelectric performance of BS–PT ceramics.

4. Conclusions

The phase structure, microstructure, dielectric, ferroelectric, and piezoelectric properties of 0.36BS–0.64PT + $x$$GeO_2$ ceramics were presented. A small amount of GeO_2 can decrease the grain size. With the increase in the GeO_2 content, the values of ε_r, d_{33}, k_p increased first and then decreased, while the values of E_C, Q_m increased monotonically. Interestingly, the Curie temperature of 0.36BS–0.64PT + $x$$GeO_2$ ceramics changes only slightly with different contents of GeO_2. The optimal composition is 0.36BS–0.64PT + 0.5 mol%GeO_2 ceramics with T_C of 455 °C, d_{33} of 385 pC N^{-1}, k_p of 58%, Q_m of 90. Compared with 0.36BS–0.64PT ceramics, the enhanced Q_m and stability of 0.36BS–0.64PT + 0.5 mol%GeO_2 ceramics is due to the addition of GeO_2. This study provides a paradigm for improving the mechanical quality factor of BS–PT-based ceramics.

Conflicts of interest

The authors declare that they have no known competing financial interests or personal relationships that could have appeared to influence the work reported in this paper.

Acknowledgements

References

1 S. J. Zhang and F. P. Yu, *J. Am. Ceram. Soc.*, 2011, **94**, 3153–3170.

2 S. Zhang, X. Jiang, M. Lapsley, P. Moses and T. R. Shrout, *Appl. Phys. Lett.*, 2010, **96**, 013506.

3 D. Damjanovic, *Curr. Opin. Solid StateMater. Sci.*, 1998, **3**, 469–473.

4 J. Wu, X. Gao, J. Chen, C.-M. Wang, S. Zhang and S. Dong, *Acta Phys. Sin.*, 2018, **67**, 207701.

5 S. J. Zhang, R. E. Eitel, C. A. Randall, T. R. Shrout and E. F. Alberta, *Appl. Phys. Lett.*, 2005, **86**, 262904.

6 J. F. Tressler, S. Alkoy and R. E. Newnham, *J. Electroceram.*, 1998, **2**, 257–272.

7 Y. Jiang, B. Qin, Y. Zhao, Y. Jiang, D. Xiao and J. Zhu, *Phys. Status Solidi RRL*, 2008, **2**, 28–30.

8 L. Fan, J. Chen, S. Li, H. Kang, L. Liu, L. Fang and X. Xing, *Appl. Phys. Lett.*, 2013, **102**, 022905.

9 S. J. Zhang, R. Xia, C. A. Randall, T. R. Shrout, R. R. Duan and R. F. Speyer, *J. Mater. Res.*, 2005, **20**, 2067–2071.

10 J. R. Cheng, W. Y. Zhu, N. Li and L. E. Cross, *Mater. Lett.*, 2003, **57**, 2090–2094.

11 R. E. Eitel, C. A. Randall, T. R. Shrout, P. W. Rehrig, W. Hackenberger and S. E. Park, *Jpn. J. Appl. Phys.*, 2001, **40**, 5999–6002.

12 C. J. Stringer, T. R. Shrout, C. A. Randall and I. M. Reaney, *J. Appl. Phys.*, 2006, **99**, 024106.

13 W. M. Zhu, H. Y. Guo and Z. G. Ye, *Phys. Rev. B*, 2008, **78**, 014401.

14 R. E. Eitel, S. J. Zhang, T. R. Shrout, C. A. Randall and I. Levin, *J. Appl. Phys.*, 2004, **96**, 2828–2831.

15 R. E. Eitel, C. A. Randall, T. R. Shrout and S. E. Park, *Jpn. J. Appl. Phys.*, 2002, **41**, 2099–2104.

16 J. Liu, *Ceram. Int.*, 2022, **48**, 3390–3396.

17 J. Liu, S. Liu and Y. Wu, *J. Alloys Compd.*, 2022, **895**, 162725.

18 T. S. H Yamazak, W. Sakamoto and T. Yago, *J. Ceram. Soc. Jpn.*, 2010, **118**, 631–635.

19 S. Zhang, Y. Yu, J. Wu, X. Gao, C. Huang and S. Dong, *J. Alloys Compd.*, 2018, **731**, 1140–1145.

20 J. Chen, H. Shi, G. Liu, J. Cheng and S. Dong, *J. Alloys Compd.*, 2012, **537**, 280–285.

21 M. D. Drahus, P. Jakes, E. Erdem, S. Schaab, J. Chen, M. Ozerov, S. Zvyagin and R. A. Eichel, *Phys. Rev. B*, 2011, **84**, 064113.

22 S. J. Zhang, E. F. Alberta, R. E. Eitel, C. A. Randall and T. R. Shrout, *IEEE Trans. Ultrason. Ferroelectr. Freq. Control.*, 2005, **52**, 2131–2139.

23 B. Deng, Q. Wei, C. He, Z. Wang, X. Yang and X. Long, *J. Alloys Compd.*, 2019, **790**, 397–404.

24 J. Chen, Y. Dong and J. Cheng, *Ceram. Int.*, 2015, **41**, 9828–9833.

25 J. Chen, G. Jin, C.-M. Wang, J. Cheng and D. Damjanovic, *J. Am. Ceram. Soc.*, 2014, **97**, 3890–3896.

26 Z. Lan, J. Liu, S. Ren, X. Jiang, K. Chen, L. Fang, B. Peng, D. Wang and L. Liu, *J. Mater. Sci.*, 2019, **54**, 13467–13478.

27 P. Kantha, N. Pisitpipathsin, K. Pengpat, S. Eitssayeam, G. Rujijanagul, R. Gua and A. S. Bhalla, *Mater. Res. Bull.*, 2012, **47**, 2867–2870.

28 F. Mou, A. Xue, Q. Liu, S. Peng, Y. Wang, E. Cai and S. Wang, *J. Mater. Sci.: Mater. Electron.*, 2021, **32**, 2432–2440.

29 K. Chen, F. Zhang, Y. Jiao, D. Li, J. Tang, F. Gao, L. An and G. Brennecka, *J. Am. Ceram. Soc.*, 2016, **99**, 1681–1686.

30 F. Zeng, Q. Liu, S. Peng, Y. Wang, E. Cai, A. Xue and S. Zhou, *Ceram. Int.*, 2019, **45**, 1416–1419.

31 W. M. Zhu and Z. G. Ye, *Appl. Phys. Lett.*, 2006, **89**, 232904.

32 X. G. Tang, K. H. Chew and H. L. W. Chan, *Acta Mater.*, 2004, **52**, 5177–5183.

33 T. Shi, L. Xie, L. Gu and J. Zhu, *Sci. Rep.*, 2015, **5**, 8606.

34 S. W. Gotmare, S. O. Leontsev and R. E. Eitel, *J. Am. Ceram. Soc.*, 2010, **93**, 1965–1969.

35 J. G. Wu, X. Chen, Z. Q. Chu, W. L. Shi, Y. Yu and S. X. Dong, *Appl. Phys. Lett.*, 2016, **109**, 173901.

36 J. G. Wu, H. D. Shi, T. L. Zhao, Y. Yu and S. X. Dong, *Adv. Funct. Mater.*, 2016, **26**, 7186–7194.